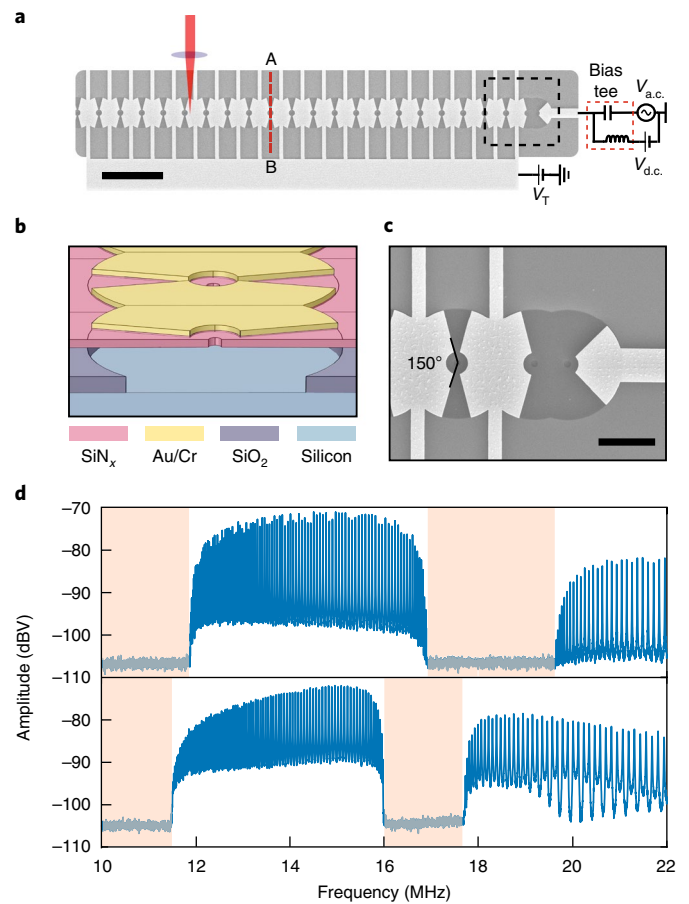


# Electrical tuning of elastic wave propagation in nanomechanical lattices at MHz frequencies

Jinwoong Cha <sup>1,2</sup> and Chiara Daraio <sup>2\*</sup>

Nanoelectromechanical systems (NEMS) that operate in the megahertz (MHz) regime allow energy transducibility between different physical domains. For example, they convert optical or electrical signals into mechanical motions and vice versa<sup>1</sup>. This coupling of different physical quantities leads to frequency-tunable NEMS resonators via electromechanical non-linearities<sup>2–4</sup>. NEMS platforms with single- or low-degrees of freedom have been employed to demonstrate quantum-like effects, such as mode cooling<sup>5</sup>, mechanically induced transparency<sup>5</sup>, Rabi oscillation<sup>6,7</sup>, two-mode squeezing<sup>8</sup> and phonon lasing<sup>9</sup>. Periodic arrays of NEMS resonators with architected unit cells enable fundamental studies of lattice-based solid-state phenomena, such as bandgaps<sup>10,11</sup>, energy transport<sup>10–12</sup>, non-linear dynamics and localization<sup>13,14</sup>, and topological properties<sup>15</sup>, directly transferrable to on-chip devices. Here we describe one-dimensional, non-linear, nanoelectromechanical lattices (NEML) with active control of the frequency band dispersion in the radio-frequency domain (10–30 MHz). The design of our systems is inspired by NEMS-based phonon waveguides<sup>10,11</sup> and includes the voltage-induced frequency tuning of the individual resonators<sup>2–4</sup>. Our NEMLs consist of a periodic arrangement of mechanically coupled, free-standing nanomembranes with circular clamped boundaries. This design forms a flexural phononic crystal with a well-defined bandgap, 1.8 MHz wide. The application of a d.c. gate voltage creates voltage-dependent on-site potentials, which can significantly shift the frequency bands of the device. Additionally, a dynamic modulation of the voltage triggers non-linear effects, which induce the formation of a phononic bandgap in the acoustic branch, analogous to Peierls transition in condensed matter<sup>16</sup>. The gating approach employed here makes the devices more compact than recently proposed systems, whose tunability mostly relies on materials' compliance<sup>17,18</sup> and mechanical non-linearities<sup>19–22</sup>.

Our NEML consists of Si-rich silicon nitride ( $\text{SiN}_x$ ) membranes ( $\sim 10\ \mu\text{m}$  in diameter) that form a phononic crystal with periodic, curved boundaries (Fig. 1a).  $\text{SiN}_x$ , an insulator, is used to separate electrically the excitation and the tuning electrodes. Neighbouring membranes are overlapped to create mechanical coupling (Fig. 1a,c). We constructed membrane arrays with variable numbers of repeating units (Supplementary Fig. 2). The periodicity of the lattice,  $a$ , was chosen to be  $7\ \mu\text{m}$  owing to the expected frequency dispersion, with prominent acoustic and optical branches separated by a well-defined phononic bandgap (Fig. 1d). To examine the effects of the tuning electrodes, we fabricated NEMLs with and without tuning electrodes and measured their frequency responses using a laser interferometer (Methods). To characterize the devices, flexural motion of the membranes was triggered by simultaneously applying



**Fig. 1 | Non-linear NEML.** **a**, Scanning electron microscope image of the non-linear NEML. Simultaneously applying  $V_{\text{d.c.}}$  and  $V_{\text{a.c.}}$  voltages to the excitation electrode via a bias tee triggers flexural motions electrostatically.  $V_{\text{T}}$  is a tuning gate voltage applied to the tuning electrodes to activate on-site electrostatic potentials. A homebuilt, balanced homodyne interferometer measures the membrane motions at desired locations. Scale bar,  $10\ \mu\text{m}$ . **b**, Schematic of the cross-section A–B marked in **a**. The thickness of the metal electrodes and the sacrificial oxide are 50 and 140 nm, respectively. A highly doped n-type silicon substrate serves as an electrical ground plane. **c**, A magnified scanning electron microscope image of the dashed square box in **a** shows the region near the excitation electrodes. Scale bar,  $5\ \mu\text{m}$ . **d**, Frequency response of the lattices with 120 unit cells. The upper (lower) panel presents the response of the device without (with) electrodes. The shaded area indicates the frequency stop bands.

<sup>1</sup>Department of Mechanical and Process Engineering, ETH Zurich, Zurich, Switzerland. <sup>2</sup>Engineering and Applied Science, California Institute of Technology, Pasadena, CA, USA. \*e-mail: [daraio@caltech.edu](mailto:daraio@caltech.edu)

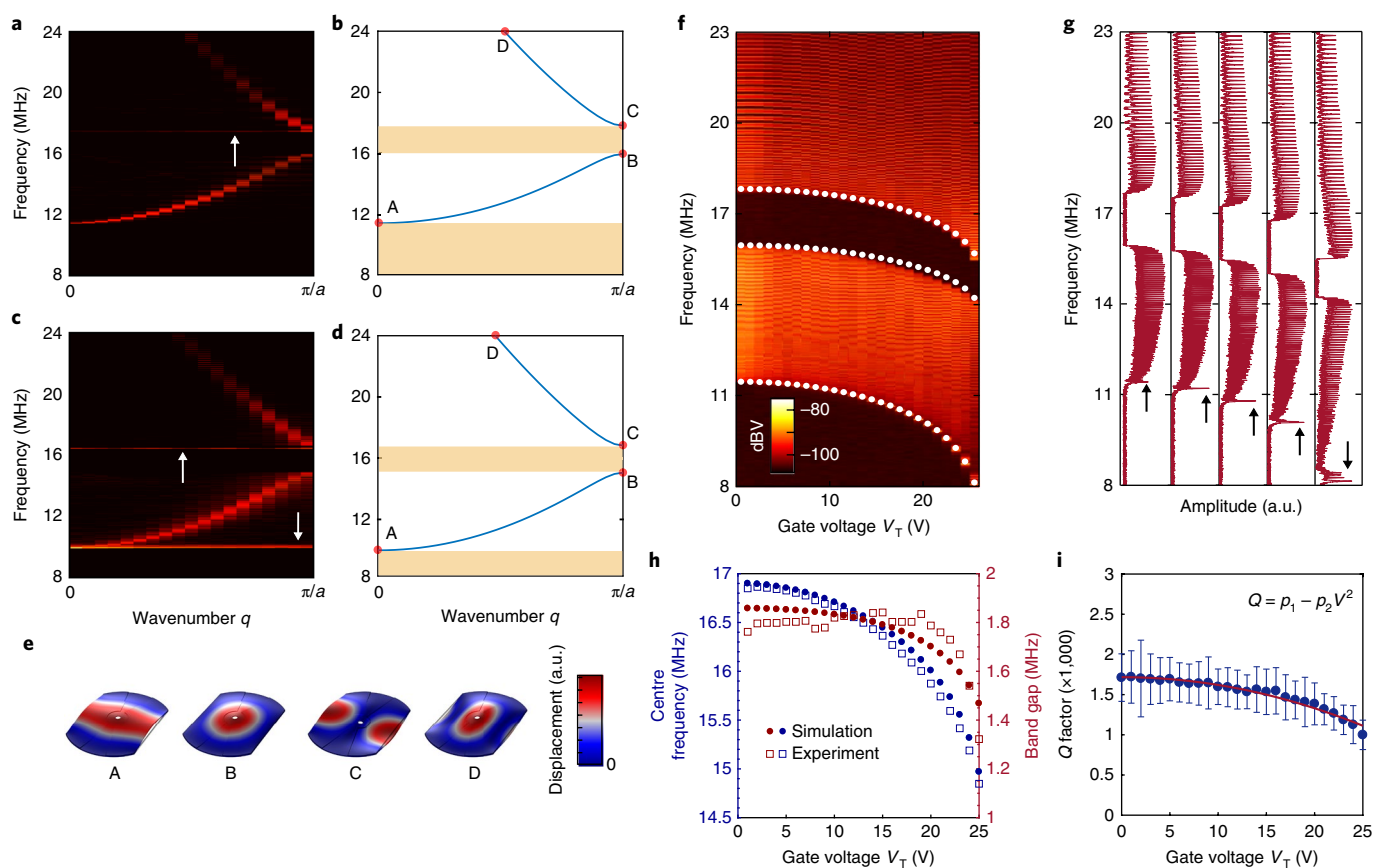


**Fig. 2 | Static tuning with a d.c. gate voltage.** **a, c**, Experimental frequency dispersion curves for  $V_{d.c.} = 2$  V and  $V_{a.c.} = 40$  mV with  $V_T = 0$  V (**a**) and 20 V (**c**). The two upward-pointing arrows in **a** and **c** indicate the defect mode of the excitation unit in the front end of the lattice. The bottom white arrow in **c** indicates several modes excited by parasitic couplings between the excitation and tuning electrodes. **b, d**, Numerical frequency dispersion curves that correspond to **a** and **c**. The light yellow regions indicate the stop bands. **e**, Mode shapes of a unit cell at different frequencies A, B, C and D marked in **b** and **d**. **f**, Experimental frequency responses of the NEML at different applied gate voltages that range from  $V_T = 0$  to 25 V. Here  $V_{d.c.} V_{a.c.} = 0.08$  V<sup>2</sup> is kept constant. The white dots denote the corresponding numerical band edges at  $q = 0$  and  $q = \pi/a$ . **g**, Frequency responses that vary  $V_T$  from 5 to 25 V with 5 V steps (left to right). The black arrows indicate the long-wavelength modes that stem from the parasitic coupling between the excitation and tuning electrodes. **h**, Position of the bandgap centre and size as a function of  $V_T$ . The red and blue squares (dots) denote the experimental (numerical) data for the bandgap centre and bandgap frequencies, respectively. **i**, Averaged Q factor from the frequency responses as a function of  $V_T$ . The Q factors are calculated by averaging  $f_0/\Delta f$  of the individual peaks in the frequency spectra for different values of  $V_T$ . Here  $f_0$  and  $\Delta f$  are the centre frequency and full-width at half-maximum, respectively, of a resonance peak. The error bars represent the s.d. of the resonance peaks for each  $V_T$ . The Q factor shows a  $Q \approx -V^2$  scaling with the fitting parameters  $p_1 = 1,717$  and  $p_2 = 0.9670$ . a.u., arbitrary units.

d.c. ( $V_{d.c.}$ ) and a.c. ( $V_{a.c.}$ ) voltages (Fig. 1a). The frequency responses of the NEMLs without and those with electrodes present clear stop bands below 12 MHz and 11.5 MHz, respectively (Fig. 1d). The NEML without electrodes has a bandgap from 17 MHz to 19.8 MHz, whereas the NEML with electrodes has a bandgap from 16 MHz to 17.8 MHz, which confirms that the gold electrodes do not significantly change the operating frequencies. Passband spectra show discrete peaks due to the finite number of unit cells ( $N = 120$ ). We performed frequency response measurements with varying number of unit cells ( $N = 30, 60, 90$  and  $120$ ) and observed well-defined phononic bandgaps even at the lowest unit cell numbers (Supplementary Fig. 3). The average quality factor (Q factor) of the device with (without) electrodes is 1,700 (3,700) and depends on the surface and the intrinsic material loss due to the evaporated gold<sup>23</sup>.

To study the phononic dispersion, we performed numerical simulations using COMSOL Multiphysics (Methods). The experimental dispersion curves, obtained from fast-Fourier transformation of the spatially scanned data, capture the phononic behaviour of our NEML (Supplementary Fig. 4). The experimental results show good agreement with numerical simulations (Fig. 2a–d) for 0 and 20 V gating voltages ( $V_T$ ), which correctly capture the location

and the size of pass and stop bands. Flat band regions exist near the band edges, at  $q = 0$  and  $\pi/a$ , which suggests slow, near-zero group velocities. The locally clamped boundaries, which act as grounding springs, cause the acoustic band edge at  $q = 0$  to start from finite frequencies. To investigate systematically the dependence of the transmission properties on the applied  $V_T$ , we measured the frequency response of the last resonator (located on the opposite boundary from the excitation) while varying the  $V_T$  from 0 to 25 V (Fig. 2f). We note a broadening of the acoustic branch from 4.5 MHz at  $V_T = 0$  V to 6 MHz at  $V_T = 25$  V and a decrease of the bandgap size from 1.8 MHz at  $V_T = 0$  V to 1.3 MHz at  $V_T = 25$  V. The experimentally measured variations of the centre frequency and the bandgap match well the numerical data from the finite element models (Fig. 2f, h). The small discrepancy observed between the experiments and numerical simulations in Fig. 2h is probably due to parasitic electrostatic effects in the experiments that are not captured in the finite element model. We characterize the Q factor as a function of the gating voltage of the NEML and show that it decreases quadratically due to dielectric losses (Fig. 2i).

To explain the experimental observations, we developed an analytical reduced-order model of the finite samples based on discrete

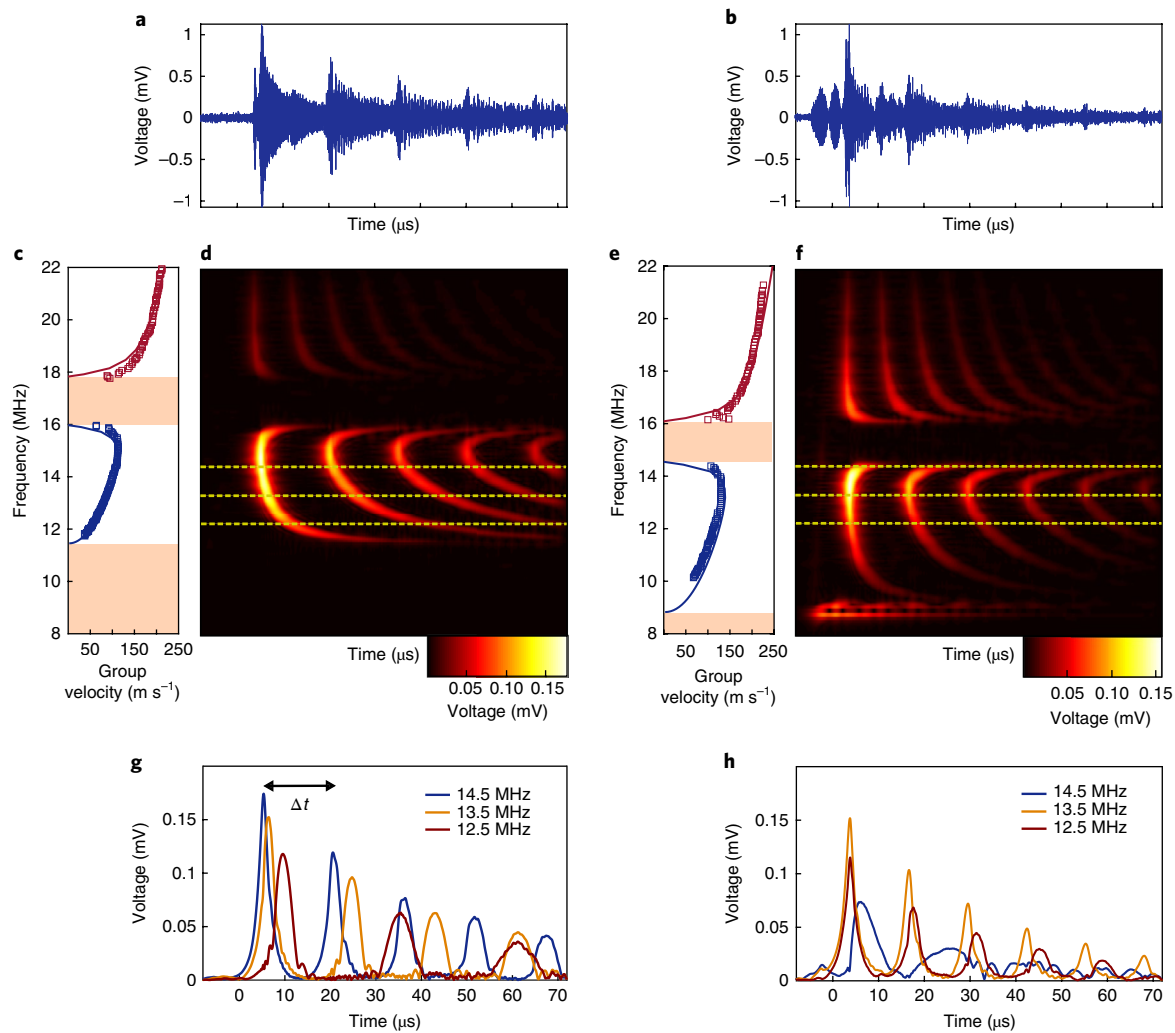


**Fig. 3 | Tunable phonon propagation velocity.** **a,b**, Transient responses of the displacement of the end resonator for two tuning gate voltages,  $V_T = 0$  V (**a**) and 24 V (**b**), prior to the signal filtering process. A chirped signal with frequency content that ranged from 8 MHz to 22 MHz was applied to the excitation electrode with  $V_{d.c.} = 20$  V and  $V_{chirp,peak} = 375$  mV. Here  $V_{d.c.}$  and  $V_{chirp,peak}$  are the d.c. voltage and the amplitude of the chirped signal, applied to the excitation electrode. **c,e**, Group velocity as a function of the centre frequency of an enveloped pulse for  $V_T = 0$  V (**c**) and 24 V (**e**). The blue and red solid lines in **c** and **e** represent the group velocities for the acoustic and optical branches obtained from numerical simulations. The dotted open squares are the corresponding experimental group velocities obtained by calculating the time of flight of a single round trip of a single pulse at different frequencies. **d,f**, The colour maps represent the time-domain amplitude responses of signal envelopes at different frequencies for  $V_T = 0$  V (**d**) and 24 V (**f**). We applied a Butterworth filter at single frequencies with 200 kHz bandwidth to filter out the broadband transient signals in **a** and **b**. Due to the increased a.c. parasitic coupling, several long-wavelength modes were excited at around 9 MHz before the pulses arrived at the end unit, as shown in **f,g,h**. Time-domain pulse envelopes at 12.5 MHz, 13.5 MHz and 14.5 MHz that correspond to the three yellow dashed lines in **d** and **f**, respectively.  $\Delta t$  is the time of flight of an envelope.

interconnected rigid plates (Supplementary Fig. 5). This model clarifies the interplay of the experimental parameters and their effect on the dispersion response of the NEML. To understand the role of residual stress on the dynamic response of the lattice, we compared the discrete model to finite element simulations. We show that the residual stress decreases the contrast of the rotational couplings, which reduces the bandgap size (Supplementary Figs. 6 and 7). The presence of a gate voltage below the membrane acts as an on-site potential that tunes the transmission. An increase of the electrostatic force applied by the tuning electrodes softens the on-site potentials and consequently downshifts the frequency bands (Supplementary Fig. 7b). The voltage-induced gap narrowing is due to the relatively complex geometry of the electrodes (not captured in the discrete model). This causes a mode-dependent softening effect in which the optical band edge at  $q = \pi/a$  presents a more drastic decrease than the acoustic band edge as the gate voltage increases

(Fig. 2h). We also use the discrete model to study the possible effects of fabrication-induced disorder (Supplementary Figs. 8 and 9), and show that the system is sensitive to the presence of random defects. However, the experimental results show a robust response (Supplementary Fig. 4), similar to theoretical results obtained from a perfect lattice. We conclude that inhomogeneities do not play an important role in our experimental system.

The tunability of the dispersion response means that the transmissible frequencies can be dynamically selected, but also that the group velocity can be controlled. This is evident from the transient responses of the lattice at  $V_T = 0$  V and 24 V (Fig. 3a,b). We sent a chirped pulse with frequencies between about 8 and 22 MHz through the lattice and measured the responses of the end unit. The measured response contained several displacement pulses, which originate from boundary reflections. To analyse the dispersive behaviours at single frequencies, we applied a Butterworth

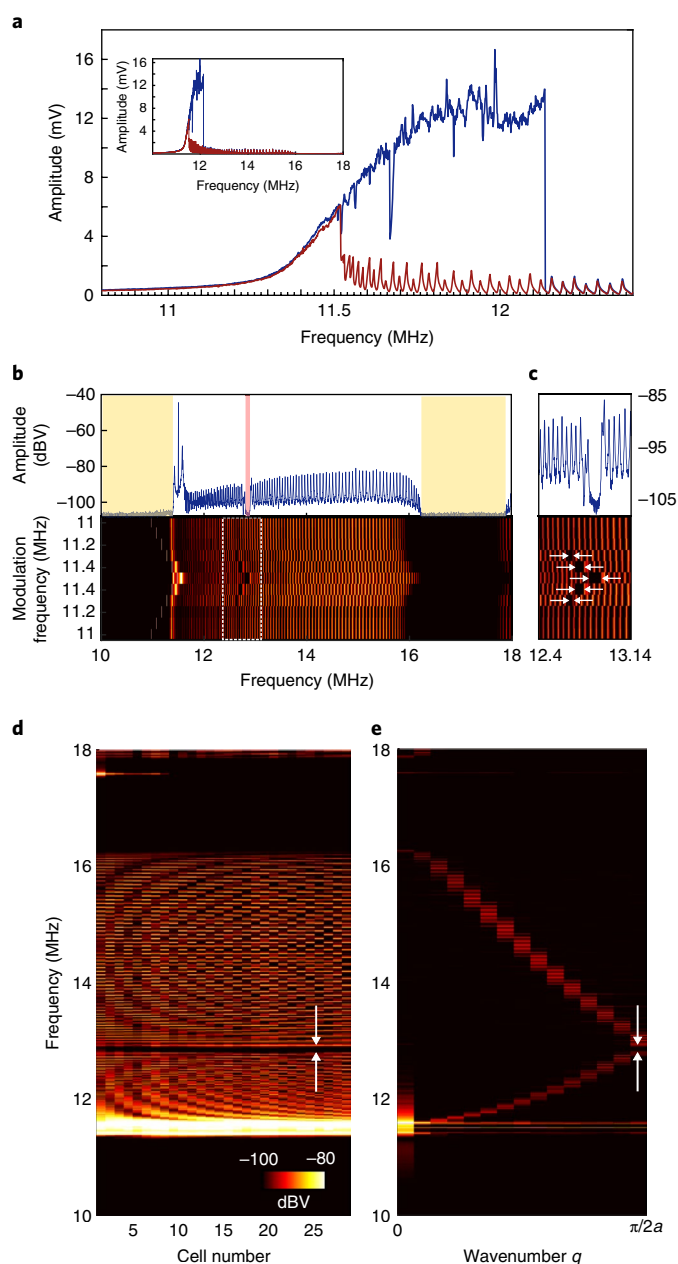


**Fig. 4 | Dynamic modulation and formation of a non-linear bandgap. a**, Frequency responses obtained when the tuning electrodes are non-linearly driven at  $V_{d.c.} = V_{T,d.c.} = 5$  V,  $V_{a.c.} = 0$  mV and  $V_{T,a.c.} = 100$  mV. Here  $V_{T,d.c.}$  and  $V_{T,a.c.}$  are the d.c. and a.c. voltages, respectively, to the tuning electrodes. The blue (red) solid line denotes a forward (backward) frequency sweep. The modes in the pass bands can be excited due to the a.c. coupling with the excitation electrode. Inset: broad band frequency responses that range from 10 to 18 MHz. **b**, Top panel: frequency response of the lattice subject to a dynamic modulation with a modulation frequency  $\omega_p = 11.5$  MHz, with  $V_{d.c.} = V_{T,d.c.} = 5$  V,  $V_{a.c.} = 10$  mV and  $V_{T,a.c.} = 100$  mV. The yellow shaded regions are the original bandgap and the pink region indicates the dynamically induced bandgap. Bottom panel: the colour map shows the frequency responses at different modulation frequencies that range from 11 to 11.5 MHz, with 1 MHz steps. We performed a forward and backward sweep of the modulation frequency to check the hysteresis. **c**, Close-up view of the data in the white dashed box in **b** and the corresponding frequency responses. **d**, Spatially scanned data along the 28 sites in the lattice. The bright regions at low frequency originate from the strong dynamic modulation. **e**, Frequency dispersion curves that correspond to the scanned data in **d**. The induced bandgap is highlighted by white arrows in **c–e**.

filter with a 200 kHz bandwidth to the broadband responses. We then plot the envelope of the filtered pulses in the time domain at each frequency (Fig. 3d,f). The time of flight of the wave near the band edges is much longer than that in the middle of the pass bands, which confirms the strong dispersion near the band edges. The experimental group velocity is obtained by calculating the velocity of the travelling pulses ( $v_g$ ) at each frequency, using  $v_g = 2Na/\Delta t$  (Fig. 3c,e). Here  $N = 120$  is the number of unit cells,  $a$  is the periodicity and  $\Delta t$  is the time of flight. The factor 2 accounts for a round trip of a pulse. The experimental group velocities show excellent agreement with the numerical group velocities. The envelope of waves near the acoustic band edge (14.5 MHz) broadens due to dispersion. The propagation losses are deduced from the amplitude decay of two neighbouring pulses at 13.5 MHz and are found to be around 33% in voltages or 56% in energy per 1.68 mm travelled, which is equivalent to  $2.1$  dB  $\text{mm}^{-1}$ . At 12 MHz, the pulse speed at  $V_T = 24$  V is about twice the pulse speed at  $V_T = 0$  V, which demonstrates group velocity tuning.

Metamaterials under dynamic environments have shown many interesting features, for example, non-reciprocity<sup>24</sup> and non-equilibrium phenomena<sup>25</sup>. We investigated the behaviour of our system under dynamic a.c. tuning. In addition to the a.c. voltage, we applied a 5 V d.c. voltage to the tuning electrode to increase the modulation amplitude. This d.c. voltage is small enough not to induce significant softening effects. As the tuning electrode simultaneously excites the entire lattice, we expect their modulation to predominantly affect the lowest modes in the phononic band. We note that the a.c. tuning triggers non-linear dynamic phenomena in the NEML, which leads to a classic hysteretic behaviour (Fig. 4a). The resonance curves show a hardening behaviour due to tension induced non-linearity. Beyond the bifurcation point, at modulation frequencies ( $\omega_p$ ) above 11.3 MHz, a small bandgap emerges in the acoustic branches (Fig. 4b,c). The gap size increases with increasing modulation frequency, changing its position. The shift of bandgap originates from the upshift of the entire dispersion curves due to the stronger tension induced at higher modulation frequencies. The presence of the modulation-induced bandgap is also evident in the real-space scanning data obtained at  $\omega_p = 11.5$  MHz, with a  $2a = 14$   $\mu\text{m}$  scanning step (Fig. 4d). Analysis of the corresponding dispersion curve confirms the effective ‘dimerization’ of the unit cell, with a gap at the new band edge  $q = \pi/2a$  (Fig. 4e), at a centre frequency around 12.7 MHz. The nonlinear second harmonics of the modulation frequency, generated due to the broken out-of-plane symmetry of the deflected membranes<sup>26</sup>, lies at  $q = \pi/2a$  in the optical branch. Accordingly, the modes’ amplitudes at  $q = \pi/2a$  have  $2a$  periodicity, which causes the dimerization (Supplementary Figs. 10–12). This non-linear bandgap formation is analogous to the Peierls transition<sup>16</sup> in solid-state systems. We performed a perturbation analysis using the discrete element model to show the emergence of the non-linear bandgap (Supplementary Fig. 13).

Here we demonstrate the static and dynamic control of NEMs by electrostatic forces. Their frequency dispersion can be tuned over a wide range by applying a d.c. gate voltage. The d.c. tuning can be used to shift the band edges, reduce the width of the bandgap and control the group velocity. Dynamic a.c. modulation of the gate shows a new mechanism for bandgap formation, induced by non-linear effects. NEMs with controllable, local on-site potentials contribute to the development of functional, miniaturized high-frequency acoustic components, such as sensors<sup>27</sup>, tunable filters and delay lines for radio-frequency signal processing applications<sup>28,29</sup>, with a smaller footprint compared to the electromagnetic counterparts. For applications in quantum technologies<sup>30,31</sup> that require low loss, the Q factor could be enhanced by replacing the gold electrodes with graphene<sup>32</sup>, increasing the residual stress of the film, and operating in cryogenic environments.

**Online content**

Any methods, additional references, Nature Research reporting summaries, source data, statements of data availability and associated accession codes are available at <https://doi.org/10.1038/s41565-018-0252-6>.

Received: 14 March 2018; Accepted: 2 August 2018;  
Published online: 10 September 2018

**References**

- Craighead, H. G. Nanoelectromechanical systems. *Science* **290**, 1532–1535 (2000).
- Chen, C. et al. Performance of monolayer graphene nanomechanical resonators with electrical readout. *Nat. Nanotech.* **4**, 861–867 (2009).
- Chen, C. et al. Graphene mechanical oscillators with tunable frequency. *Nat. Nanotech.* **8**, 923–927 (2013).
- Bagci, T. et al. Optical detection of radio waves through a nanomechanical transducer. *Nature* **507**, 81–85 (2014).
- Mahboob, I., Nishiguchi, K., Okamoto, H. & Yamaguchi, H. Phonon-cavity electromechanics. *Nat. Phys.* **8**, 387–392 (2012).
- Okamoto, H. et al. Coherent phonon manipulation in coupled mechanical resonators. *Nat. Phys.* **9**, 480–484 (2013).
- Faust, T., Rieger, J., Seitner, M. J., Kotthaus, J. P. & Weig, E. M. Coherent control of a classical nanomechanical two-level system. *Nat. Phys.* **9**, 485–488 (2013).
- Mahboob, I., Okamoto, H., Onomitsu, K. & Yamaguchi, H. Two-mode thermal-noise squeezing in an electromechanical resonator. *Phys. Rev. Lett.* **113**, 167203 (2014).
- Mahboob, I., Nishiguchi, K., Fujiwara, A. & Yamaguchi, H. Phonon lasing in an electromechanical resonator. *Phys. Rev. Lett.* **110**, 127202 (2013).
- Hatanaka, D., Mahboob, I., Onomitsu, K. & Yamaguchi, H. Phonon waveguides for electromechanical circuits. *Nat. Nanotech.* **9**, 520–524 (2014).
- Hatanaka, D., Dodel, A., Mahboob, I., Onomitsu, K. & Yamaguchi, H. Phonon propagation dynamics in band-engineered one-dimensional phononic crystal waveguides. *New J. Phys.* **17**, 113032 (2015).
- Yu, S. et al. Surface phononic graphene. *Nat. Mater.* **15**, 1243–1247 (2016).
- Sato, M. et al. Observation of locked intrinsic localized vibrational modes in a micromechanical oscillator array. *Phys. Rev. Lett.* **90**, 044102 (2003).
- Sato, M., Hubbard, B. E. & Sievers, A. J. Colloquium: Nonlinear energy localization and its manipulation in micromechanical oscillator arrays. *Rev. Mod. Phys.* **78**, 137–157 (2006).
- Cha, J., Kim, K. W. & Daraio, C. Experimental realization of on-chip topological nanoelectromechanical metamaterials. Preprint at <https://arxiv.org/abs/1806.10680> (2018).
- Gruener, G. The dynamics of charge-density waves. *Rev. Mod. Phys.* **60**, 1129 (1988).
- Babae, S., Viard, N., Wang, P., Fang, N. X. & Bertoldi, K. Harnessing deformation to switch on and off the propagation of sound. *Adv. Mater.* **28**, 1631–1635 (2016).
- Wang, P., Casadei, F., Shan, S., Weaver, J. C. & Bertoldi, K. Harnessing buckling to design tunable locally resonant acoustic metamaterials. *Phys. Rev. Lett.* **113**, 014301 (2014).
- Boechler, N., Yang, J., Theocharis, G., Kevrekidis, P. G. & Daraio, C. Tunable vibrational band gaps in one-dimensional diatomic granular crystal with three-particle unit cells. *J. Apply. Phys.* **109**, 074906 (2011).
- Spadoni, A. & Daraio, C. Generation and control of sound bullets with a nonlinear acoustic lens. *Proc. Natl Acad. Sci. USA* **107**, 7230–7234 (2010).
- Lydon, J., Serra-Garcia, M. & Daraio, C. Local to extended transitions of resonant defect modes. *Phys. Rev. Lett.* **113**, 185503 (2014).
- Bilal, O. R., Foehr, A. & Daraio, C. Reprogrammable phononic metasurfaces. *Adv. Mater.* **29**, 1700628 (2017).
- Seitner, M. J., Gajo, K. & Weig, E. M. Damping of metallized bilayer nanomechanical resonators at room temperature. *Appl. Phys. Lett.* **105**, 213101 (2014).
- Sounas, D. L. & Alu, A. Non-reciprocal photonics based on time modulation. *Nat. Photon.* **11**, 774–783 (2017).
- Bachelard, N. et al. Emergence of an enslaved phononic bandgap in a non-equilibrium pseudo-crystal. *Nat. Mater.* **16**, 808–813 (2017).
- Eichler, A., Moser, J., Dykman, M. I. & Bachtold, A. Symmetry breaking in a mechanical resonator made from a carbon nanotube. *Nat. Commun.* **4**, 2843 (2013).
- Biswas, T. S. et al. Remote sensing in hybridized arrays of nanostrings. *Nano Lett.* **14**, 2541–2545 (2014).
- Kharrat, C. et al. Modal control of mechanically coupled NEMS arrays for tunable RF filters. *IEEE Trans. Ultrason. Ferroelectr. Freq. Control* **57**, 1285–1295 (2010).
- Olsson, R. H. III & El-Kady, I. Microfabricated phononic crystal devices and applications. *Meas. Sci. Technol.* **20**, 012002 (2009).
- Tsaturyan, Y., Barg, A., Polzik, E. S. & Schliesser, A. Ultracoherent nanomechanical resonators via soft clamping and dissipation dilution. *Nat. Nanotech.* **12**, 776–783 (2017).
- Vermersch, B., Guimond, P.-O., Pichler, H. & Zoller, P. Quantum state transfer via noisy photonic and phononic waveguides. *Phys. Rev. Lett.* **118**, 133601 (2017).
- Lee, S. et al. Graphene metallization of high-stress silicon nitride resonators for electrical integration. *Nano Lett.* **13**, 4275–4279 (2013).

**Acknowledgements**

We acknowledge partial support for this project from NSF EFRI Award no. 1741565, Binnig and Rohrer Nanotechnology Center at IBM Zurich and the Kavli Nanoscience Institute at Caltech. We thank E. Togan at ETH Zurich for his advice on interferometers.

**Author contributions**

J.C. and C.D. conceived the idea for the research. J.C. designed and fabricated the samples. J.C. built the experimental set-ups and performed the experiments. J.C. developed the analytical models and performed the numerical simulations. J.C. and C.D. analysed the data and wrote the manuscript.

**Competing interests**

The authors declare no competing interests.

**Additional information**

**Supplementary information** is available for this paper at <https://doi.org/10.1038/s41565-018-0252-6>.

**Reprints and permissions information** is available at [www.nature.com/reprints](http://www.nature.com/reprints).

**Correspondence and requests for materials** should be addressed to C.D.

**Publisher's note:** Springer Nature remains neutral with regard to jurisdictional claims in published maps and institutional affiliations.

## Methods

**Sample fabrication.** The fabrication of the NEMs began with a low-pressure chemical vapour deposition of 100 nm low-stressed SiN<sub>x</sub> on both sides of a SiO<sub>2</sub>(140 nm)/Si(525 μm) wafer. The sacrificial thermal oxide under the SiN<sub>x</sub> layer defines the vacuum gap distance when the device is released in the HF etching step. The wafer was then cleaned with acetone and isopropyl alcohol. We then spin coated 495K A4 and 950K A2 poly(methylmethacrylate) (PMMA). The electrode patterns were transferred using electron-beam (e-beam) lithography, and the PMMA resists were developed in a methyl isobutyl ketone and isopropyl alcohol mixture. An e-beam evaporator was then used to deposit 45 nm gold and 5 nm chromium layers for the e-beam alignment markers, excitation and tuning electrodes. Then, the samples were immersed in acetone for 2 h to lift off the remaining PMMA resists covered by the metals. For the next e-beam exposure, we spin coated a 500 nm ZEP520A e-beam resist to serve as an etch mask for the subsequent reactive ion etching process. A second e-beam lithography was then performed to pattern the arrays of the etch holes of diameter 500 nm and the exposed resist was developed in a ZED-N50 developer. We employed an inductively coupled plasma dry etching to drill the holes in the SiN<sub>x</sub> device layer. The remaining resist was dissolved in a *N*-methyl-2-pyrrolidone-based solvent. The wafer was then scribed into 3 mm × 3 mm dies and the dies were immersed in a buffered oxide solution to etch the sacrificial SiO<sub>2</sub> layer through the etch holes. After the etching process, we used a critical point dryer to avoid the adhesion of the released freestanding membranes to the substrates and obtained perfectly isotropic circular membranes. The SiN<sub>x</sub> is hardly etched by buffered HF (etch rate of ~0.3 nm min<sup>-1</sup>). Furthermore, the low-pressure chemical vapour deposition process led to minimal disorder and structural defects, which ensured a uniform adhesion to the sacrificial layer and a low residual stress (~100 MPa).

**Experiments.** The measurements of the mechanical motion of the membranes were performed using a homebuilt optical interferometer at room temperature and a vacuum pressure  $P < 10^{-6}$  mbar. The interferometer is a phase-locked Michelson interferometer that employs a balanced homodyne detection scheme. The phase-lock is enabled by moving a reference mirror mounted on a PID (proportional-integral-derivative)-controlled piezoelectric actuator at 1.5 kHz. The motion of the membranes was electrostatically excited by simultaneously applying d.c. and a.c. voltages through a bias tee (ZFBT-6GW+ (Mini-circuits)). A 633 nm laser light with a ~20 μW input power was incident on the sample. The reflected light interfered with the light from the reference mirror. The intensity of the interfered

light was measured using the balanced photodetector. Its radio-frequency output signal was connected to high-frequency lock-in amplifier (UHFLI (Zurich Instruments)). The position of the laser spot was monitored with a CMOS camera and the measurement position was controlled by a computer-controlled XY linear stage that supported the vacuum chamber. Supplementary Information gives details of the method.

**Numerical simulations.** All the numerical simulations to calculate the phononic frequency dispersion were performed using the finite element method via COMSOL. We employed the module prestressed eigenfrequency analysis, considering geometric non-linearities, to reflect the effect of membrane deflection and stresses induced by the d.c. gate voltage. The d.c. voltage also introduced an effective softening potential. We implemented these effects by assigning a non-linear surface load,  $F = -\epsilon_0 V^2 / 2(d_{\text{eff}} + w)$ , to the area covered by the tuning electrodes. Here  $\epsilon_0$  is the vacuum permittivity,  $V$  the tuning voltage,  $d_{\text{eff}} = 145$  nm (the effective gap distance fitted from experiments) and  $w$  the membrane's displacement. The mechanical properties used for silicon nitride films were 3,000 kg m<sup>-3</sup> density, 290 GPa Young's modulus and a 0.27 Poisson ratio. For the properties of the electrodes of 50 nm thickness, made of 45 nm gold and 5 nm chrome, we calculated the geometric averages of the properties and obtained 18,100 kg m<sup>-3</sup> density, 98 GPa Young's modulus and a 0.417 Poisson ratio. The geometric parameters of a unit cell were a 4.95 μm radius and a 7 μm periodicity. The initial thickness of SiN was set to 100 nm. We considered partial etching of SiN<sub>x</sub> due to the buffered HF by removing 14 nm thick SiN<sub>x</sub> from the top surface uncovered by the tuning electrode. The partial etching of SiN<sub>x</sub> surface above the sacrificial oxide was also considered by removing a volume of a cone with a 250 nm top radius, 4.95 μm bottom radius and 14 nm height. For the circular boundaries, we imposed fixed boundary conditions. Bloch periodicity conditions,  $u(x+a) = e^{iqa}u(x)$ , were applied to the unit cell connecting boundaries by assigning Floquet periodicity in COMSOL. Here,  $u(x)$  is the displacement at position  $x$ ,  $a$  is a periodicity and  $q$  is a wavenumber. We imposed anisotropic in-plane residual stresses of 35 MPa for the direction perpendicular to the lattice and 125 MPa for the parallel direction to match the experimental frequency dispersion (Fig. 2a). The contributions of both residual stress components are discussed in Supplementary Fig. 6.

## Data availability

The data that support the findings of this study are available from the corresponding author upon reasonable request.